Graphene-Encapsulated FeS$_2$ in Carbon Fibers as High Reversible Anodes for Na$^+$/K$^+$ Batteries in a Wide Temperature Range

Changmiao Chen, Yincai Yang, Xuan Tang, Renhua Qiu, Shuangyin Wang, Guozhong Cao, and Ming Zhang

Developing low cost, long life, and high capacity rechargeable batteries is a critical factor towards developing next-generation energy storage devices for practical applications. Therefore, a simple method to prepare graphene-coated FeS$_2$ embedded in carbon nanofibers is employed; the double protection from graphene coating and carbon fibers ensures high reversibility of FeS$_2$ during sodiation/desodiation and improved conductivity, resulting in high rate capacity and long-term life for Na$^+$ (305.5 mAh g^{-1} at 3 A g^{-1} after 2450 cycles) and K$^+$ (120 mAh g^{-1} at 1 A g^{-1} after 680 cycles) storage at room temperature. Benefitting from the enhanced conductivity and protection on graphene-encapsulated FeS$_2$ nanoparticles, the composites exhibit excellent electrochemical performance under low temperature (0 and –20 °C), and temperature tolerance with stable capacity as sodium-ion half-cells. The Na-ion full-cells based on the above composites and Na$_3$V$_2$(PO$_4$)$_3$ can afford reversible capacity of 95 mAh g^{-1} at room temperature. Furthermore, the full-cells deliver promising discharge capacity (50 mAh g^{-1} at 0 °C, 43 mAh g^{-1} at –20 °C) and high energy density at low temperatures. Density functional theory calculations imply that graphene coating can effectively decrease the Na$^+$ diffusion barrier between FeS$_2$ and graphene heterointerface and promote the reversibility of Na$^+$ storage in FeS$_2$, resulting in advanced Na$^+$ storage properties.

1. Introduction

The rapid development of portable electronics and electric vehicles have induced the demands for green, safety, and low-cost energy storage devices with high capacity, energy density, and stability.[1] Lithium-ion batteries (LIBs) have been successfully applied as commercial rechargeable batteries during the past decades, owing to its high reliability and energy density. However, it is disappointing that the limited lithium resources and uneven distribution in earth result in high cost and block the sustainable development of LIBs industry. Therefore, more and more researchers focus on exploring and designing alternative batteries that own the similar properties as LIBs. In consideration of Na$^+$ and K$^+$ with the similar chemical property as Li$^+$, they have similar redox potentials (E$_{Na^+/Na}$ = –2.71 V, E$_{K^+/K}$ = –2.92 V) to Li$^+$ (E$_{Li^+/Li}$ = –3.04 V) versus standard hydrogen electrode.[2] Therefore, sodium-ion batteries (SIBs) and potassium-ion batteries (PIBs) are considered as ideal alternatives to LIBs. However, the Na$^+$ (R$_{Na^+}$ = 1.02 Å) and K$^+$ (R$_{K^+}$ = 1.38 Å) have larger radius than Li$^+$ (R$_{Li^+}$ = 0.76 Å),[3] resulting in the materials that undergo larger strain than LIBs which may consequently suffer Na$^+$/K$^+$ storage irreversibility. Although graphite is the most well-known anode materials for LIBs and owns a theoretical capacity of 372 mAh g^{-1}, it shows very low capacity for SIBs (31 mAh g^{-1}) and PIBs (279 mAh g^{-1}, corresponding to form KC$_8$ during potassiation), which is a major barrier to the practical application.[4] Moreover, larger Na$^+$/K$^+$ brings out serious volume expansion and electrode materials degeneration during

Dr. C. Chen, Prof. M. Zhang
Key Laboratory for Micro/Nano Optoelectronic Devices
of Ministry of Education
Hunan Provincial Key Laboratory of Low-Dimensional
Structural Physics & Devices
School of Physics and Electronics
Hunan University
Changsha 410082, China
E-mail: zhangming@hnu.edu.cn

Dr. Y. Yang, Prof. R. Qiu, Prof. S. Wang
State Key Laboratory of Chemo/Biosensing and Chemometrics
Provincial Hunan Key Laboratory for Graphene Materials and Devices
College of Chemistry and Chemical Engineering
Hunan University
Changsha 410082, China

Dr. X. Tang
Clean Energy Automotive Engineering Center
Tongji University
Shanghai 201804, China

Prof. G. Cao
Department of Materials Science & Engineering
University of Washington
Seattle, WA 98195, USA

ADVANCED
SCIENCE NEWS
www.advancedsciencenews.com

NANO · MICRO
small
www.small-journal.com

the charge/discharge process, resulting in low capacity and cyclic instability.[5] Therefore, it is of great importance to design nanostructure materials that will meet with high reversible capacity, high energy density, and fast Na^+/K^+ storage.

Carbon-based materials, especially carbon nanofibers, porous carbon, graphene, graphene complex, and S/N/P doped carbon compounds, have been widely used in SIB or PIB anode materials.[6] However, most of the carbon-based materials investigated for SIBs or PIBs suffer from sluggish electrochemical properties due to the large irreversible capacity loss and unstable voltage platform, resulting in low rate capacity and charge/discharge stability. On the other hand, most transition metal oxides,[7] alloys,[8] metal phosphides,[9] and metal sulfides[10] with low conductivity suffer from volume expansion and materials collapse, resulting in inferior electrochemical properties. Among them, FeS_2 as a transition metal sulfide has risen prominent attention, owing to its natural abundance, environmental friendly character, intrinsic safety, and high theoretical capacity (894 mAh g^{-1}). Meanwhile, FeS_2 has low conductivity. More unfavorable, during the charge/discharge conversion reaction progress of FeS_2 will produce the dissolved polysulfide (S_n^{2-}). Such highly mobile S_n^{2-} ions transfer into organic liquid electrolytes, resulting in a bad electrochemical activity.[11] Thus, appropriate structural design, voltage cut-off control, and electrolyte selection are the advisable strategies to address the above issues. For example, Lou and co-workers synthesized carbon-coated FeS_2 yolk–shell nanoboxes as SIBs which showed excellent rate capacity and cycle stability. Moreover, they demonstrated that the large surface and pore volume of the nanoboxes can provide larger contact areas and more channels for the immersion of electrolyte.[12] Chen's group proved that Co-doped FeS_2 can effectively combine both the high rate capability and capacity, where the hybrid FeS_2 nanospheres revealed obvious advantages than the pure FeS_2 nanoparticles on capacity for SIBs.[13] Owing to the severe volume expansion and collapse of active materials during discharge below 0.8 V, some strategies are presented to increase the discharge cut-off voltage to address these negative effects although they will sacrifice part of specific capacity.[14] So far, great efforts have been made to improve the electrochemical performances of FeS_2-based SIBs/LIBs anode materials. Consequently, more effort in areas of nanostructure, conductivity, and ion diffusion rate of electrodes should be made to support the practical application of FeS_2-based SIBs/LIBs.[15]

In this work, we designed and synthesized a graphene-encapsulated FeS_2 nanoparticles which were embedded in carbon nanofibers (FeS_2@graphene@carbon nanofibers (FeS_2@G@CNF)) through electrospinning. The FeS_2@G@CNF composites as anodes for SIBs or PIBs showed high reversible electrochemical reaction with long cyclic life. In addition, the $Na_3V_2(PO_4)_3$ cathode materials were prepared by high-energy ball milling and calcination, which showed stable voltage platform and high capacity. When matching the FeS_2@G@CNF anode with $Na_3V_2(PO_4)_3$ cathode to assemble Na-ion full-cells, they exhibited high energy density and stable cycle performance. Especially, the FeS_2@G@CNF anodes conducted stable electrochemical performance and high capacity under low temperature, and the FeS_2//$Na_3V_2(PO_4)_3$ full-cells also owned high energy density. The study about FeS_2 anode materials may provide a potential choice for the future rechargeable batteries.

2. Results and Discussion

The synthesis procedure of FeS_2@G@CNF composite is illustrated in Figure S1 in the Supporting Information. The $Fe(acac)_3$-graphene oxide (GO)-polyacrylonitrile (PAN) precursor solution was gained by the way of electrospinning and oxidation in the air to obtain FeO_x@G@CNF, and then sulfuration in tube furnace to obtain the product of FeS_2@G@CNF. **Figure 1**a–j presents the scanning electron microscopy (SEM) and transmission electron microscopy (TEM) images of FeS_2@G@CNF and FeS_2@carbon nanofibers (FeS_2@CNF). Figure S2a–b in the Supporting Information shows that the FeS_2@G@CNF fiber mats consists of a number of interlaced nanofibers. Figure S2c,d in the Supporting Information shows the similar morphology of FeS_2@CNF which compares with FeS_2@G@CNF. There are no obvious differences between the two FeS_2 samples under the low-magnification SEM images. The enlarged picture in Figure 1a shows that the FeS_2@G@CNF nanofibers are integral and uniform. The higher resolution picture in Figure 1b clearly shows the fibers with a smooth surface and about 300 nm in diameter. For the FeS_2@CNF sample without graphene, the SEM image in Figure 1c shows that the fibers are also uniform with 300 nm in diameter, but the surface is rough. By further observing the two samples from cross-sectional SEM images in Figure S3 in the Supporting Information, there are obvious FeS_2 particles coated on the surface of the FeS_2@CNF sample, while the FeS_2@G@CNF with graphene is protected resulting in a smooth surface, indicating that graphene can affect the dimension and distribution of FeS_2 nanoparticles in carbon nanofibers. TEM image in Figure 1g shows the sample FeS_2@CNF with some dotted FeS_2 nanoparticles throughout the fiber and the surface of the fiber is rough. High-resolution TEM (HRTEM) in Figure 1h,i indicates these crystal planes belong to pyrite FeS_2. In contrast, Figure 1d shows the FeS_2@G@CNF with a smooth surface, and no obvious FeS_2 particles can be detected on the surface, which shows a different appearance from the FeS_2@CNF. This phenomenon indicates that graphene introduced into nanofibers can effectively encapsulate FeS_2, leading to no obvious detectable particles on the surface of the carbon nanofibers. The HRTEM in Figure 1e,f further proves the above phenomenon, which clearly show some graphene-encapsulated FeS_2 particles in the carbon fibers. Figure 1e gives obvious lattice fringes of 0.22 and 0.24 nm, which correspond to the (211) and (210) planes of FeS_2, respectively. The TEM element mapping of FeS_2@G@CNF in Figure 1j shows that the Fe, S, C, and N are distributed uniformly throughout the carbon nanofibers. From another perspective, the morphology characterizations indicated that graphene in nanofibers can effectively decrease the size and distribution of FeS_2 nanoparticles, which may promote the electrochemical reaction between FeS_2 and Na^+/K^+.

X-ray photoelectron spectroscopy (XPS) was carried out to confirm the chemical composition of FeS_2@G@CNF. As shown in **Figure 2**c, there are five peaks which can be attributed to C, N, O, S, and Fe, respectively. The fine spectrum of Fe 2p (Figure 2d) displays three peaks at 707.3, 711.1, and 711.5 eV, which are corresponding to the Fe^{2+} in pyrite. The peaks at ≈715.4 and ≈718 eV can be considered as the satellite peaks.[16] Other higher binding energy at 725 and ≈728.6 eV are caused by slight Fe^{3+}-S or Fe^{3+}-O on the surface of the
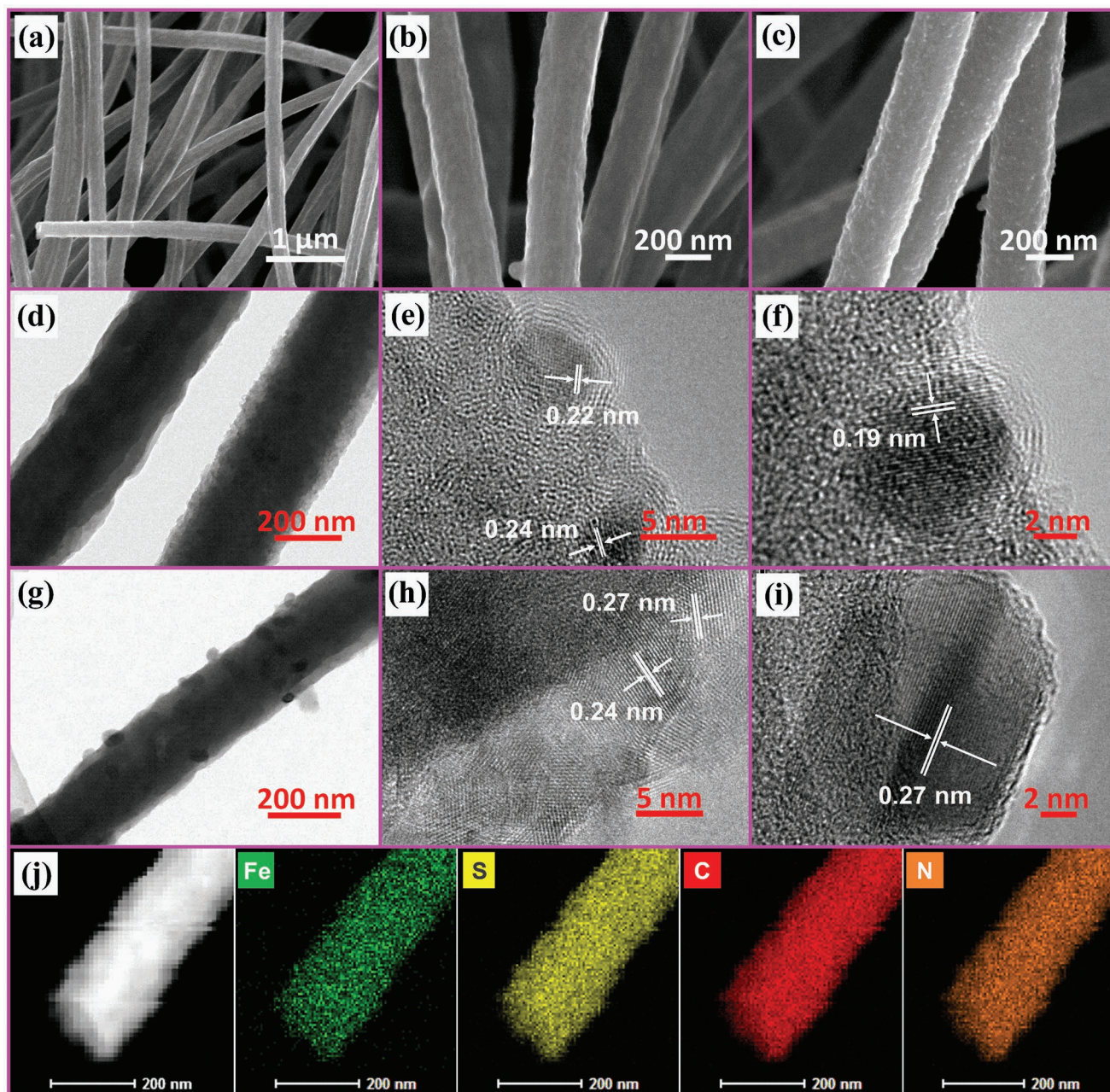
Figure 1. SEM and TEM analysis of the FeS$_2$@G@CNF and FeS$_2$@CNF. SEM images of a,b) FeS$_2$@G@CNF and c) FeS$_2$@CNF; TEM images of d–f) FeS$_2$@G@CNF show that FeS$_2$ nanoparticles are encased by graphene. g–i) TEM images of FeS$_2$@CNF. j) FeS$_2$@G@CNF TEM mappings clearly indicate that the Fe, S, C, and N elements are uniform distribution along the nanofibers.

materials.[16c] Figure 2e displays the S 2p spectrum. The peaks at 163.1 and 163.9 eV are assigned to S^{2-},[16a,b] and the higher binding energy at ≈164.6 eV arises from S$_n^{2-}$.[16c] Another two peaks at 168.5 and 169.6 eV are attributed to oxidation of S^{2-} and sulfates.[16b,17] In Figure 2f, the N 1s spectrum peaks located at 398.5, 399.9, and 401 eV demonstrate the existence of pyridinic-N, pyrrolic-N, and graphitic-N in the fiber materials.[18] This phenomenon reveals the PAN as precursors leading to the N element unavoidably doped in carbon.[19] Furthermore, Figure 2a shows the X-ray diffraction (XRD) of FeS$_2$@CNF and FeS$_2$@G@CNF. There is a broad peak around

25°, corresponding to the (002) plane of disordered carbon. The other obvious peaks appeared from 28.5° to 56.3° can be indexed as pure pyrite FeS$_2$ (JCPDS No. 42-1340). No other impurity peaks can be observed, suggesting that there are no other iron compounds in the material. The Raman spectrum in Figure 2b shows two peaks at 1356 and 1596 cm^{-1}, relating to the D and G bands of carbon, which are associated to the disordered amorphous carbon and crystalline graphic carbon, respectively.[20] The I_D/I_G for FeS$_2$@G@CNF and FeS$_2$@CNF are 1.47 and 1.58, respectively. The relative low I_D/I_G ratio of FeS$_2$@G@CNF indicates that graphene can enhance the

ADVANCED
SCIENCE NEWS
www.advancedsciencenews.com
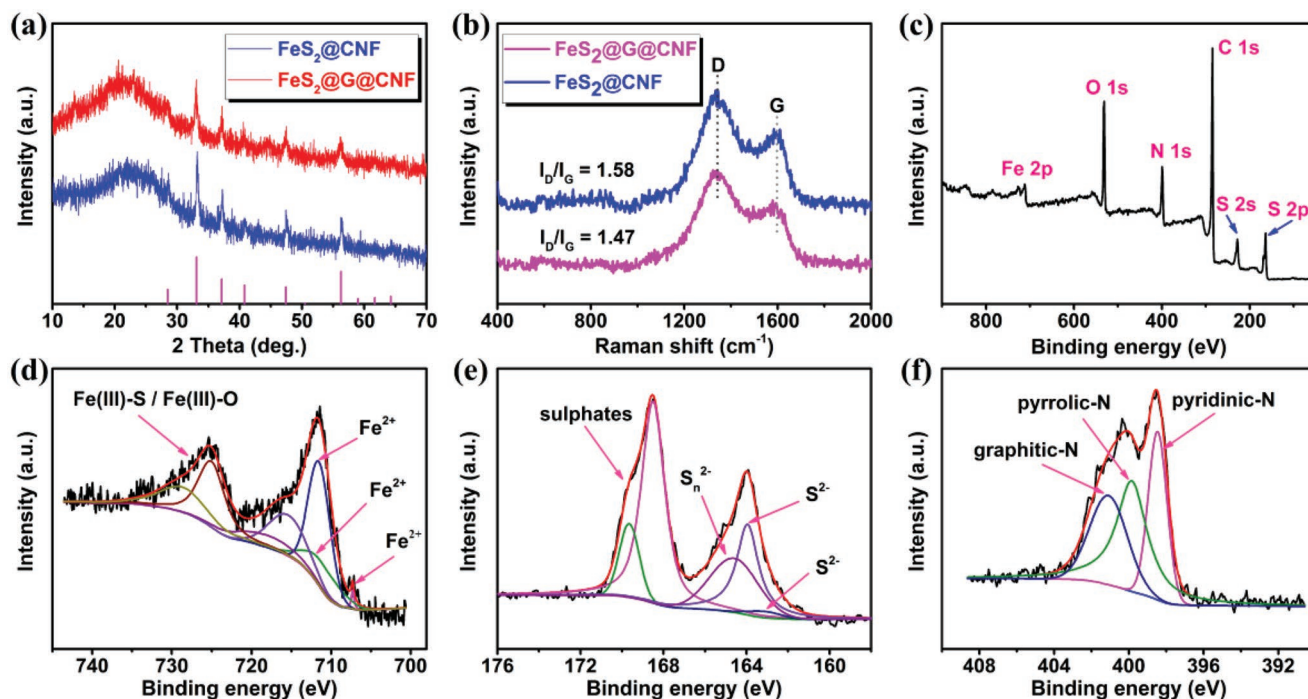
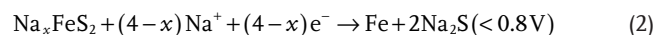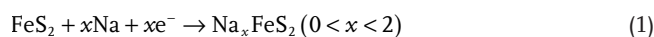NANO · MICRO
small
www.small-journal.com

Figure 2. The photoelectron spectroscopy analysis of the FeS_2 anode materials. a) XRD and b) Raman shift of $FeS_2@G@CNF$ and $FeS_2@CNF$. c) XPS survey spectrum of $FeS_2@G@CNF$, and the high-resolution spectrum of d) Fe 2p, e) S 2p, and f) N 1s.

graphitization degree of carbon fibers. All the aforementioned morphology and photoelectron spectroscopy characterizations indicated the successful synthesis of graphene-coated FeS_2 nanoparticles in the carbon nanofibers. Moreover, it has demonstrated that graphene not only can control the diameter and distribution of FeS_2 in carbon fibers, but also influence the graphitization degree and conductivity of composites.

To elucidate the morphology and composite impact on the electrochemical properties of the as-prepared FeS_2/carbon materials, we tested the materials via coin-type half-cells. The electrochemical impedance spectroscopy (EIS) in Figure S4 in the Supporting Information was performed to analyse the electrochemical behavior of as-prepared FeS_2/carbon materials. All the Nyquist plots include a high-frequency semicircle corresponding to the charge-transfer resistance (R_{ct}) between electrode and electrolyte, and the low-frequency region with straight lines attributed to the Warburg resistance (Z_w), which reflects the diffusion of Na^+ in the electrode materials. $FeS_2@G@CNF$ is with an $R_{ct} = 90\ \Omega$ and $FeS_2@CNF$ exists as a larger semicircle ($R_{ct} = 170\ \Omega$) in high-frequency region, indicating the graphene added can enhance the charge-transfer impedance to improve materials conductivity and promote the fast electrochemical reaction kinetics. **Figure 3**a shows the cyclic voltammetry (CV) results of $FeS_2@G@CNF$ as SIB anodes. In the first cathodic scan, a sharp peak is observed at about 1.0 V, which is attributed to the decomposition of electrolyte and the irreversible formation of solid electrolyte interphase (SEI) film on the surface of electrode materials.[21] From the second cycle, two broad peaks at 2.0 and 0.4 V can be related to the Na^+ insertion peaks and multi-step reaction mechanism.[21b,22] The subsequent anodic peaks located at 1.3, 2.0, and 2.5 V are corresponding to the desodiation. Those phenomena can be

summarized as the reaction between Na^+ and FeS_2 at relatively high voltages to form Na_xFeS_2 ($x < 2$) and transform into Fe and Na_2S at lower voltages.[22] The procedures will be reversed during the charge, $Fe + Na_2S$ to form Na_2FeS_2 at lower voltages, and with the increasing the voltage, Na^+ gradually extracts to form $Na_{2-x}FeS_2$ ($0 < x < 2$). The Na^+ storage mechanism can be presented as follows:

$$FeS_2 + xNa + xe^- \rightarrow Na_xFeS_2\ (0 < x < 2) \tag{1}$$

$$Na_xFeS_2 + (4-x)Na^+ + (4-x)e^- \rightarrow Fe + 2Na_2S\ (<0.8\,V) \tag{2}$$

There is a similar CV curve of $FeS_2@CNF$ in Figure S5a in the Supporting Information, showing the same Na^+ storage mechanism of pyrite in $FeS_2@CNF$. The summation of the integrated area of the peaks current is less than the first cycle, indicating the irreversible reaction and capacity loss. This is in accord with the galvanostatic charge/discharge curves in Figure 3b. $FeS_2@G@CNF$ shows the initial discharge and charge capacity of 640 and 454 mAh g^{-1}, corresponding to the first coulombic efficiency of 71%. The cells showed a slow capacity decrease in subsequent cycles, and the capacity maintained at about 420 mAh g^{-1} after 100 cycles. The $FeS_2@CNF$ showed no obvious capacity change in the first 80 cycles (Figure S6a, Supporting Information), similar to $FeS_2@G@CNF$, whereas a serious capacity decay during the latter cycles was observed, showing an inferior stability. The rate capability in Figure 3c gives the trend that with the increasing of current density from 0.1 to 3 A g^{-1}, the specific capacity decays gradually. Although $FeS_2@G@CNF$ and $FeS_2@CNF$ have no evident distinction in capacity at the low current densities (<1 A g^{-1}), there
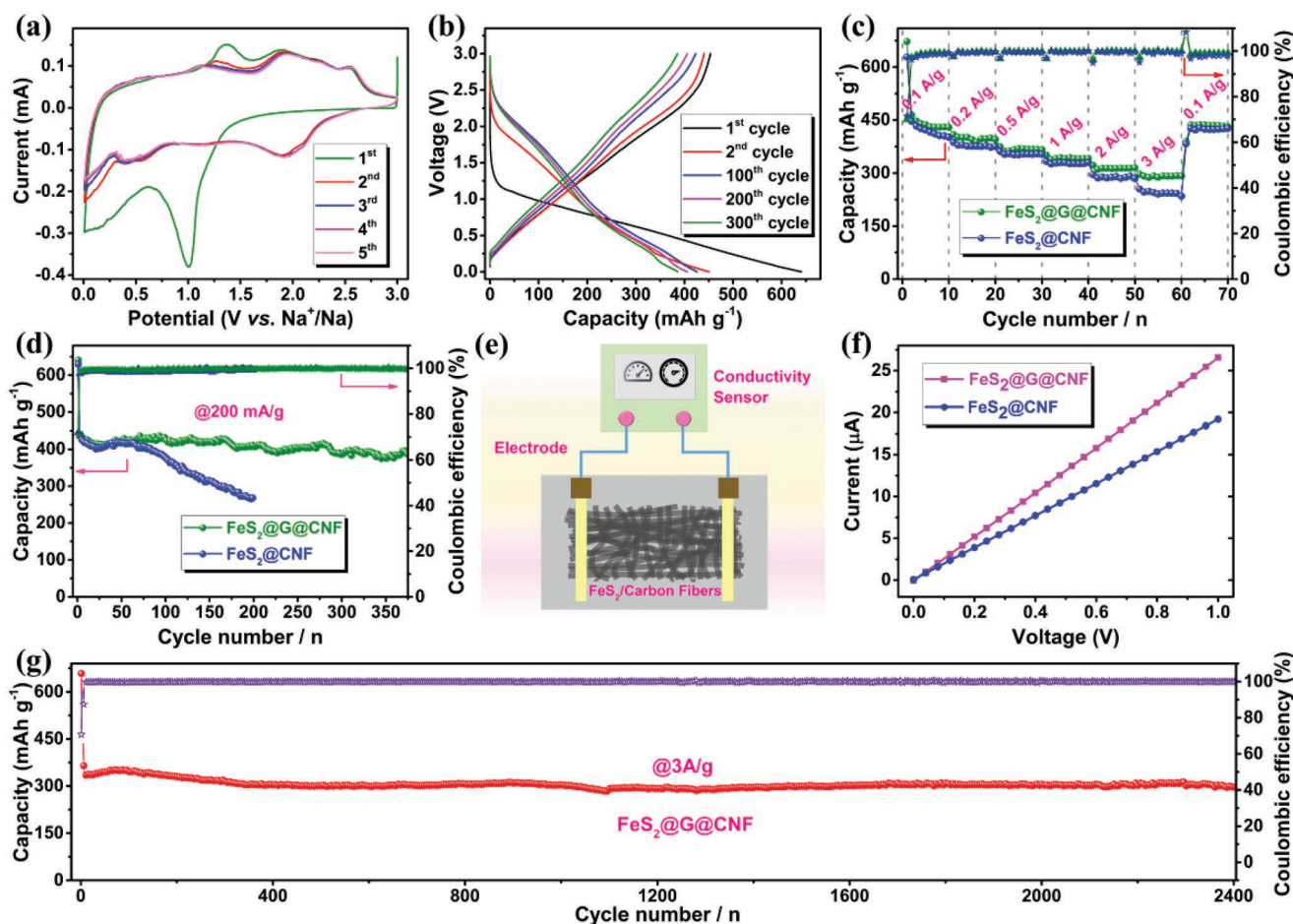
ADVANCED
SCIENCE NEWS
www.advancedsciencenews.com

NANO · MICRO
small
www.small-journal.com

Figure 3. Electrochemical Na^+ storage properties. a) CV curves of FeS_2@G@CNF under 0.1 mV s^{-1}; b) charge/discharge profiles of FeS_2@G@CNF at 200 mA g^{-1}; c) rate capacity comparison between FeS_2@G@CNF and FeS_2@CNF from 0.1 to 3 A g^{-1}; d) discharge capacities of FeS_2@G@CNF and FeS_2@CNF at 200 mA g^{-1}; e,f) I–V test of FeS_2@G@CNF using the fibrofelt ($L \times W = 2 \times 1$ cm) between 0 and 1 V; g) long-term cyclic stability and the corresponding coulombic efficiency of FeS_2@G@CNF at 3 A g^{-1}.

is an obvious superiority for FeS_2@G@CNF when increasing the current to 2 and 3 A g^{-1}. This further indicates that graphene coating can protect and enhance the conductivity of FeS_2, resulting in ultrafast electron transport rate. Furthermore, when the current returns to 0.1 A g^{-1}, both of them can obtain the original capacity, reflecting the good reversibility. The cyclic stability and specific capacity are shown in Figure 3d. FeS_2@G@CNF exhibited a stabilized capacity after 370 cycles, which owned an average capacity of 400 mAh g^{-1} and the capacity retention was 91.2%. Meanwhile, the coulombic efficiency achieved nearly 100%. In spite of that the FeS_2@CNF obtained about 400 mAh g^{-1} within the initial dozens of cycles, it decreased to below 300 mAh g^{-1} after 150 cycles. The above comparisons between FeS_2@G@CNF and FeS_2@CNF confirm the high reversibility of FeS_2@G@CNF SIBs anodes under the protection of graphene and the enhanced conductivity of the anode materials. The I–V method is schematically shown in Figure 3e, and the result is displayed in Figure 3f. It clearly shows the FeS_2@G@CNF with bigger slope in I–V curve, which means smaller resistance than that of FeS_2@CNF. In particular, Figure 3g displays the long-time properties of FeS_2@G@CNF at a current density of 3 A g^{-1} after the initial

five cycles at 0.1 A g^{-1}. The discharge capacity remains as high as 305.5 mAh g^{-1} after 2450 cycles, and the capacity retention is about 93%, suggesting outstanding properties of FeS_2@G@CNF among the reported Fe-based sulfide (Table S1, Supporting Information).[23] Moreover, to further investigate the Na^+ storage mechanism, a subsistent surface-controlled effect (capacitive contribution) process has been thoroughly considered. As shown in Figure S7 in the Supporting Information, the FeS_2@G@CNF electrode reveals diffusion-controlled (battery effect) and surface-limited process (capacitive effect) which are results of the interaction that promotes the enhanced Na^+ storage behavior. The electrode materials after 200 cycles were disassembled and observed by SEM. Figure S8 in the Supporting Information shows the FeS_2@G@CNF with a smooth surface and uniform structure, while the FeS_2@CNF with obvious sags and crests surface along the fragmentary fibers, attesting the more stable structure and Na^+ storage ability for FeS_2@G@CNF. The above analysis shows that the high reversible electrochemical reaction between FeS_2@G@CNF and Na^+ profited from the highly conductive fibers network and graphene-coated FeS_2 nanoparticles with good protection.
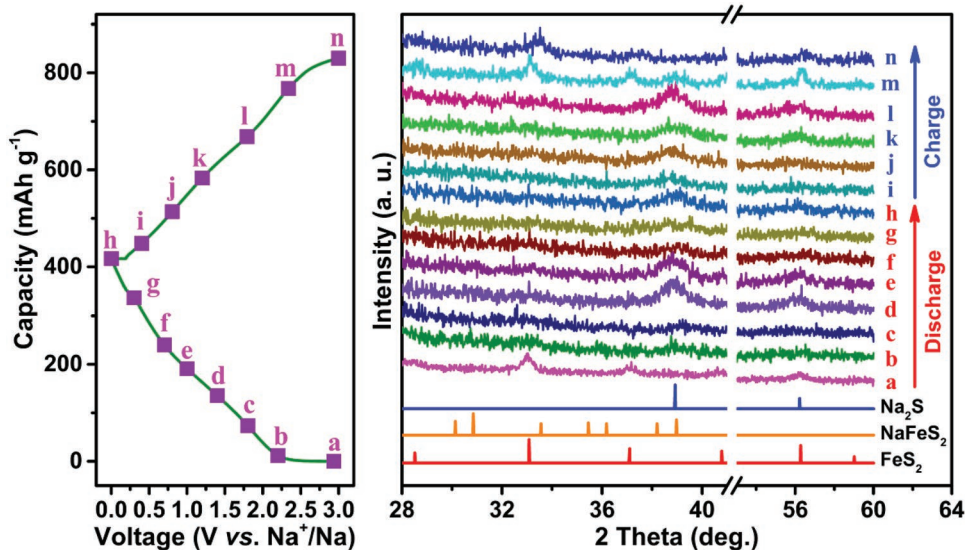
Figure 4. The ex situ XRD patterns of FeS_2@G@CNF as Na-ion battery anodes during the discharge and charge process.

To trace the evolutions of FeS_2 during the sodiation/desodiation, ex situ XRD was carried out to test the sample for the second cycle at 50 mA g^{-1}. As shown in **Figure 4**, the first full charged electrode is in accord with FeS_2, which will fade away in the following discharge process and the Na_2S and $NaFeS_2$ peaks will appear, when voltage downs near 0 V and the complete Na_2S is produced. However, in the desodiation process, Na_2S can be completely converted to FeS_2. This result confirms the reaction mechanism as described in Equations (1) and (2) consisting with the conclusion of the CV test. From another point, the ex situ XRD reflects a highly reversible electrochemical reaction of the anode material; this may benefit from the graphene-coated FeS_2 nanoparticles that facilitate conversion reactions for Na^+ storage,[22] which will ensure enhanced Na^+ storage performance.

From mobile devices to smart grids, it is important for a battery to work stably under a wide temperature range. **Figure 5**a shows that the FeS_2@G@CNF owns the reversible capacity of 250 and 200 mAh g^{-1} at 0 and −20 °C, respectively. The electrode materials tested at −20 °C after 100 cycles is uniform and
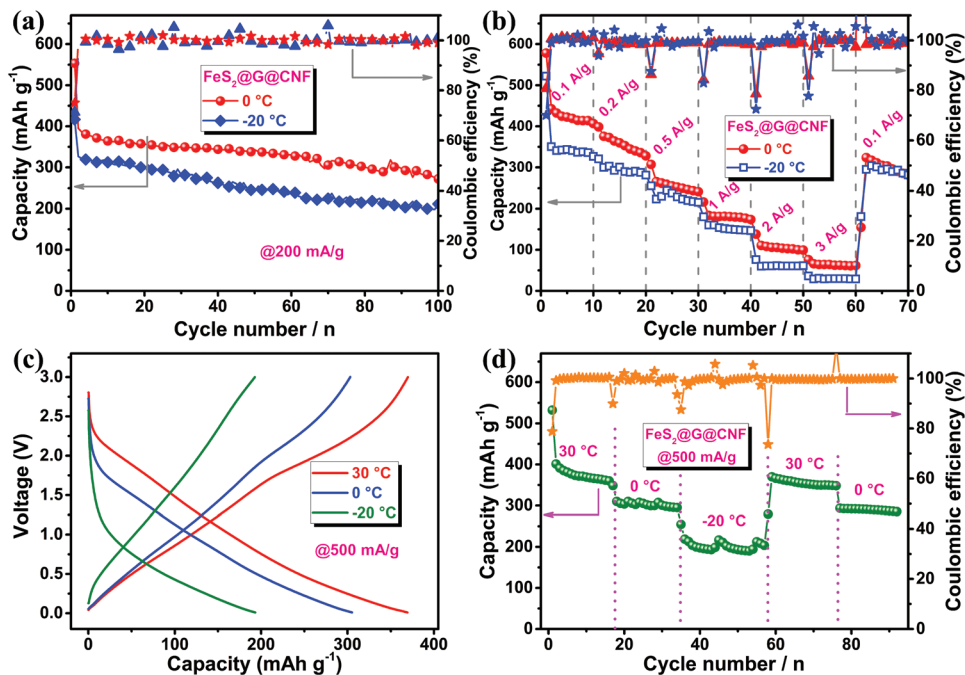

Figure 5. The electrochemical properties of FeS_2@G@CNF as anodes for SIBs at 0 and −20 °C. a,b) Long-time stability and rate capacities at 0 and −20 °C; c) charge/discharge curves from 30 to −20 °C at 0.5 A g^{-1}; d) discharge capacity under the successive temperature changing at 0.5 A g^{-1}.

**ADVANCED
SCIENCE NEWS**

www.advancedsciencenews.com

**NANO · MICRO
small**

www.small-journal.com

complete (Figure S9, Supporting Information), showing strong structural stability under very low temperature. When increased the current gradually from 0.1 to 3 A g^{-1} (Figure 5b), the capacity of FeS$_2$@G@CNF decreased from 420 to 65 mAh g^{-1} at 0 °C and from 340 to 30 mAh g^{-1} at −20 °C. With the current resetting to 0.1 A g^{-1}, the capacity recovered to approximate initial value quickly. This result reveals the prominent Na$^+$ storage ability for FeS$_2$@G@CNF at very low temperature. Figure 5c shows the charge/discharge curves at 30, 0, and −20 °C. With the dropping of temperature, the charge platform will increase and it decreases in the associated discharge process, which shows greater dynamics under the low temperature. Figure 5d shows the FeS$_2$@G@CNF with outstanding temperature tolerance. The SIBs system still stay a stable state under sharp change in temperature from 30 to −20 °C, and it proves that FeS$_2$@G@CNF has the application prospect in low-temperature system again. The low-temperature Na$^+$ storage behavior will provide a reliability for the practical application under an extreme environment.

The K$^+$ storage property of the pyrite (FeS$_2$) is also investigated in this work. The electrochemical tests were performed with half-cells and the voltage range was 0.01–3.0 V. The CV curves of FeS$_2$@G@CNF in **Figure 6**a show two cathodic peaks at 1.1 and 0.7 V under 0.1 mV s^{-1} in the first scan. They disappear at 1.1 V in the subsequent cycles, indicating the

irreversible K$^+$ insertion and the formation of SEI in the initial cycle. Two pairs of redox peaks at 1.8/2.5 and 0.7/1.4 V were found in the following scan, which corresponded to the potassiation and depotassiation process. What is noteworthy is that the shapes and areas of these peaks remain almost unchanged during sequential scans, suggesting a reversible redox reaction. Figure S5b in the Supporting Information reveals the CV curves of FeS$_2$@CNF, suggesting a similar electrochemical mechanism to FeS$_2$@G@CNF. There are no evident charge/discharge plateaus in these plots for K-ion/Na-ion batteries, which would attribute to the nano-size effect among these nanostructure materials[24]; the same phenomenon was reported in some recent reported works.[15f,25] Figure 6b shows the typical charge/discharge profiles of PIBs at various current densities. With the increase of current densities, the rate capacity gradually decreases, which can be ascribed to the relatively larger polarization upon higher current rates.[26] Figure 6c further represents the rate capability of FeS$_2$@nanofibers at different rates. The anode of FeS$_2$@G@CNF shows the discharge capacity of 406, 332, 243, and 171 mAh g^{-1} at the current density of 0.1, 0.2, 0.5, and 1 A g^{-1}, respectively. When the current density was back to lower value, the capacity can regain the initial values, indicting its high reversibility. Obviously, the FeS$_2$@CNF shows an inferior K$^+$ storage ability compared to FeS$_2$@G@CNF from the rate performance, which is in accord with the next
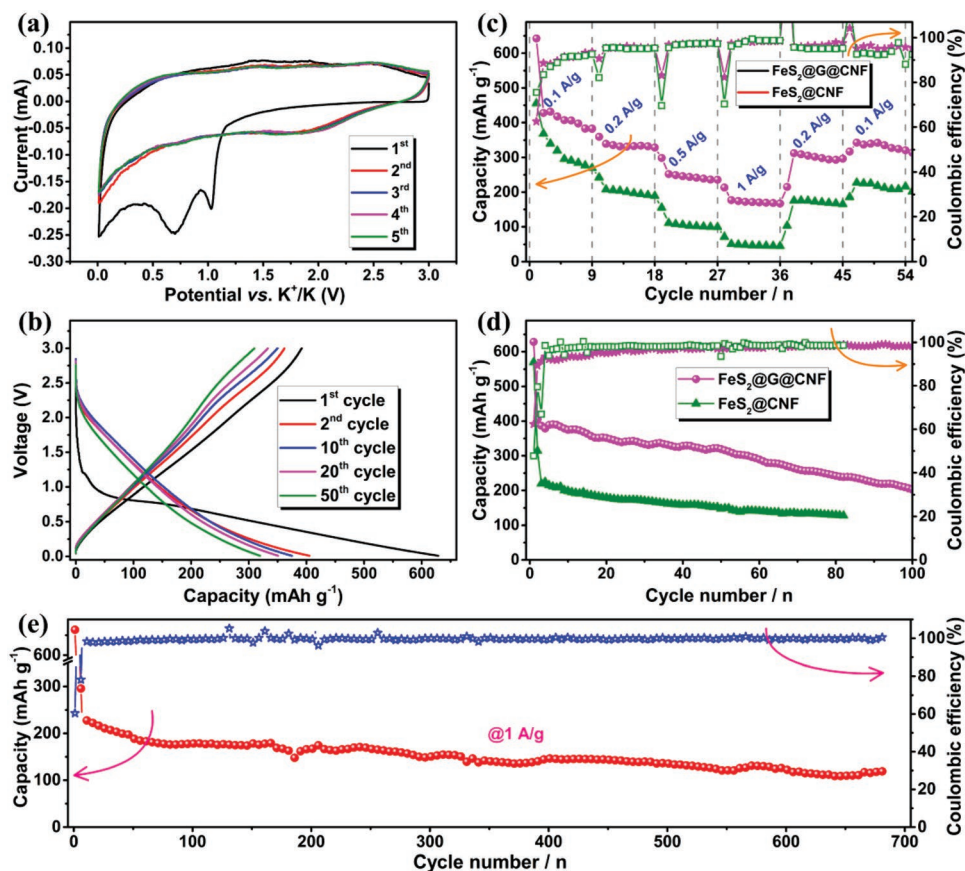

Figure 6. The K$^+$ storage properties of FeS$_2$@G@CNF. a) CV curves at 0.1 mV s^{-1}; b) charge/discharge profiles of FeS$_2$@G@CNF; c) rate capacities of FeS$_2$@G@CNF and FeS$_2$@CNF from 0.1 to 1 A g^{-1}; d) cyclic stability and revisible capacity at 200 mA g^{-1}; e) long-term properties of FeS$_2$@G@CNF at 1 A g^{-1}.

ADVANCED
SCIENCE NEWS
www.advancedsciencenews.com

NANO · MICRO
small
www.small-journal.com

cycle performance. In Figure 6d, the FeS$_2$@G@CNF material can obtain a capacity more than 300 mAh g^{-1} in the previous 50 cycles, and it felled to 205 mAh g^{-1} after 100 cycles, showing a reasonable capacity on K$^+$ storage. Although the FeS$_2$@CNF delivers a high capacity as FeS$_2$@G@CNF in the foremost 10 cycles, it decays to below 200 mAh g^{-1} in the several follow-up cycles rapidly and its coulombic efficiency is less than 90%, which shows untoward K$^+$ storage behavior. In order to evaluate the high rate capacity of FeS$_2$@G@CNF, the current density was increased to 1 A g^{-1}. Figure 6e shows that the capacity of FeS$_2$@G@CNF at 1 A g^{-1} can remain at around 120 mAh g^{-1} with an excellent coulombic efficiency even after 680 cycles. It is obtained ≈62% capacity retention after 680 cycles, which proves the stable cyclability of the FeS$_2$@G@CNF as anode for PIBs. More importantly, the FeS$_2$@G@CNF anode material exhibits improved K$^+$ storage specialty at low temperature (Figure S10, Supporting Information), and the discharge capacity can achieve ≈150 mAh g^{-1} at 200 mA g^{-1} under 0 °C. Also, the rate capability shows that the capacity can quickly recover to initial value (185 mAh g^{-1} at 100 mA g^{-1}) after high current density test, which indicates the admirable K$^+$ storage property at wide temperature just like in SIBs.

To further research the properties of FeS$_2$@G@CNF, it is necessary to find a suitable cathode to assemble full-cells. Na$_3$V$_2$(PO$_4$)$_3$ (NVP) has attracted much more attention as one of the most promising cathode materials for SIBs due to the NASICON-type open 3D framework with a fast ion-diffusion transportable channels, favorable thermal stability, relatively high operating voltage, and high energy density.[27] According to previous studies, NVP/C composites were synthesized by solid ball milling and calcination under high temperature.

The as-prepared NVP exhibited a discharge capacity of 107 mAh g^{-1} at 1 C; even it can deliver 72 mAh g^{-1} under 20 C and maintain 65 mAh g^{-1} after 1500 cycles (all the images and electrochemical characterizations are available in Figures S11–S17, Supporting Information).

Even though we have made a progress in the anodes and cathodes applied in half-cells and have proved their advantages in electrochemical performance at high rates, especially, it should be more significant to promote the practical application of FeS$_2$@G@CNF than just declaring its good electrochemical performance in half-cells. So, full-cells based on FeS$_2$@G@CNF as anodes and NVP/C as cathodes were assembled. Figure S18 in the Supporting Information shows the working schematic of full-cells, where Na$^+$ deintercalates from the NVP crystals and go through the electrolyte to react with the FeS$_2$ in the charging process. Considering the charge/discharge platform of FeS$_2$@G@CNF anodes usually below 2.5 V and NVP cathodes with a platform of 3.4 V in the discharge, and 3.6 V during the charge process, we set a voltage between 0.6 and 3.6 V. Figure S19 in the Supporting Information displays the charge/discharge profile of the FeS$_2$@G@CNF‖NVP Na-ion full-cells at 1 C (the capacity estimate based on the NVP cathodes in coin-cell), which can clearly see a voltage platform with slope from 3.0 to 1.0 V. The discharge capacity is 108 mAh g^{-1} and the charge/discharge voltage platform is stable, revealing a reliable electrochemical performance in Na-ion full-cell. **Figure 7**a presents the discharge capacity on high rates of 0.5, 1, 2, 5, 10, and 20 C and the full-cells can deliver the discharge capacity of 110, 107, 103, 94, 78, and 46 mAh g^{-1}, respectively. When the current density decreases to 0.5 C, the capacity can recover to the initial value. Those results clearly show that the
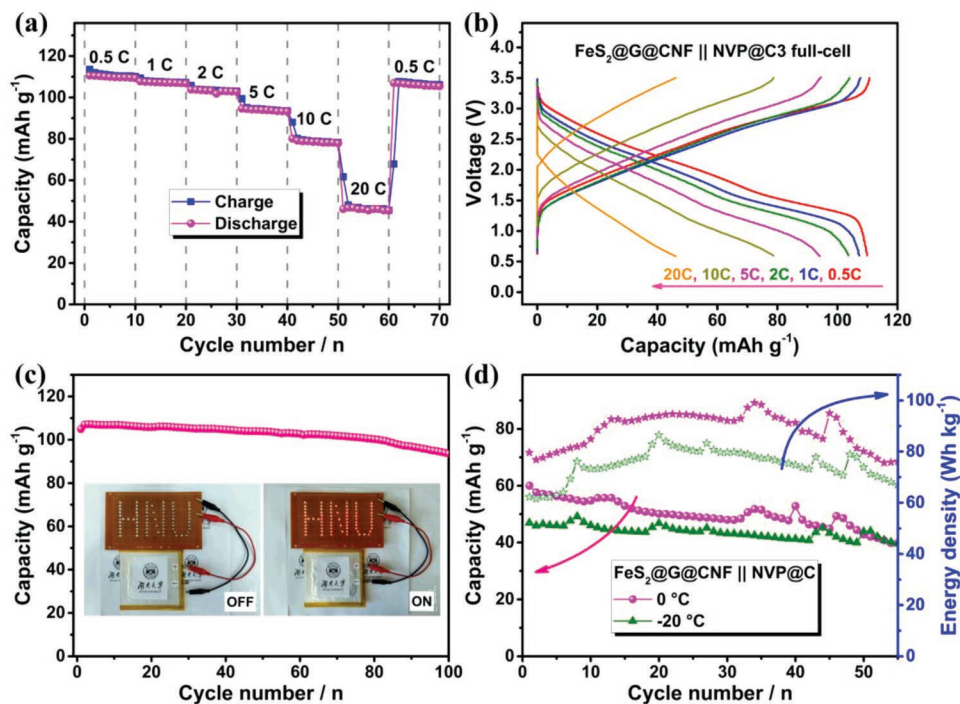

Figure 7. The electrochemical tests of FeS$_2$@G@CNF‖NVP@C3 full-cells between 0.6 and 3.6 V. a) Charge/dischage capacity in the current density range of 0.5 to 20 C; b) charge/discharge profiles from 0.5 to 20 C; c) the 100 cycles capacity under 1 C (the inset digital photographs show the "HNU" Logo which has been lighted up before and after); d) discharge capacity and energy density of the full-cells under 0 and −20 °C.
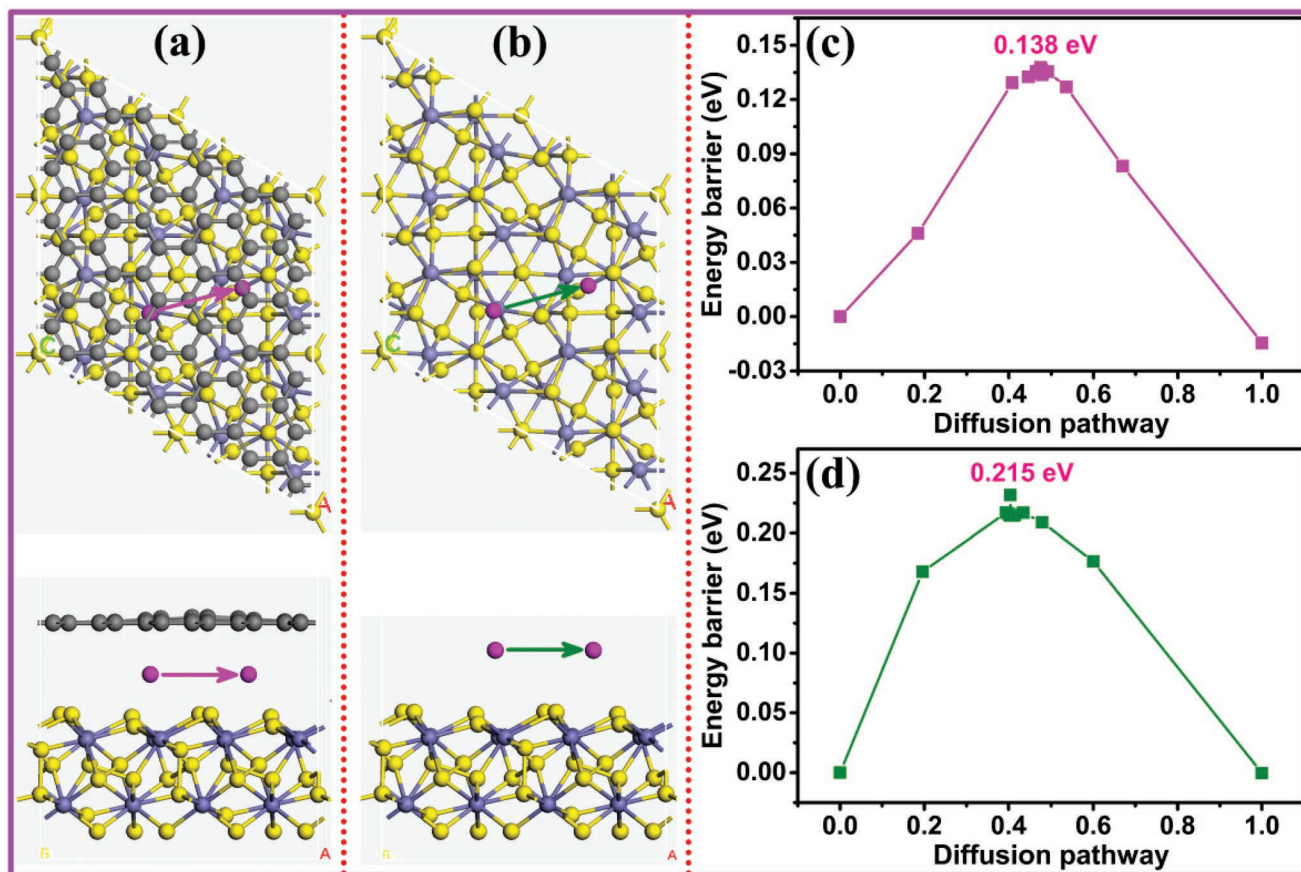
Figure 8. The Na atoms diffusion energy barrier between FeS_2 and graphene. a,b) Na atoms migrate under the FeS_2/graphene heterointerface and the surface of single FeS_2, respectively. c,d) Energy barrier of the both conditions; obviously, the Na atom has lower barrier (0.138 eV) between the FeS_2/graphene heterointerface than on the surface of simplex FeS_2 surface (0.215 eV).

capacity and dependability in full-cells are as outstanding as in half-cells. Figure 7b shows the charge/discharge profiles from 0.5 to 20 C. Along with the increasement of current densities, the potential polarization will rise gradually and the voltage platform is recognizable, which indicates a high stability of the electrochemical behavior in full-cells. Figure 7c shows cycle properties of the full-cells, and the average reversible capacity is 102 mAh g^{-1} after 100 cycles. Moreover, the energy density of FeS_2//NVP full-cells in the primary discharge progress can reach ≈150 Wh kg^{-1}; after 100 cycles, the energy density can stay above 100 Wh kg^{-1} (Figure S20, Supporting Information). To appraise the possible practical applications of the full-cells, Ragone plots (Figure S21, Supporting Information) reflecting the relationship between specific energy and power were carried out to compare with the reported Na-ion full-cells and their hybrid devices. As shown in the plots, the $Na_3V_2(PO_4)_3$‖FeS_2 can exhibit a high energy density of 169 Wh kg^{-1} at the power density of 88 W kg^{-1}, and it still displayed an impressive power density of 2176 W kg^{-1} at the energy density of 45 Wh kg^{-1}. Although our device is not the best among the reported works, it possesses absolute advantage compared to most of others. Considering the abundant resources and low cost of FeS_2, the Na-ion full-cell based on FeS_2@G@CNF in this work will be a very promising candidate to build a battery with both high

energy density and high power density. A noticeable phenomenon is that the full-cells exhibited the capacities of 50 and 43 mAh g^{-1} even at 0 and −20 °C (Figure 7d), respectively. The average energy densities in the first 50 cycles are 58.7 and 50.1 Wh kg^{-1} at 0 and −20 °C, respectively. Therefore, the Na^+ full-cells showed credible performance for practical application at both room environment and low temperatures.

To further validate the potential application, the assembled Na-ion full-cells were used to light up commercial LED bulbs (red light). Figure 7c (inset) shows that the "HNU" Logo consisted of 75 multiple LED bulbs that can be easily light up by a pouch-type full-cell or a full charged coin-cell (Figure S22, Supporting Information). Surprisingly, the pouch-type full-cells can even drive a miniature electro-motor (Video, Supporting information). The outstanding performance of full-cells could be attributed to the stable structure and low resistance during the charge/discharge process. Hence, these results demonstrated the as-prepared FeS_2/NVP is a promising SIBs applied candidate with high energy density and long cyclic life, which will be a potential advanced energy storage device for the next generation.

It is demonstrated that transition metal sulfide combined with graphene can effectively enhance the Na^+ storage electrochemical performance by theoretical calculation.[28] In order to

ADVANCED
SCIENCE NEWS
www.advancedsciencenews.com

NANO · MICRO
small
www.small-journal.com

further reveal the Na$^+$ storage behavior and the conductivity of FeS$_2$ by graphene introduced into the composite, density functional theory (DFT) calculations with Cambridge Sequential Total Energy Package (CASTEP) methods had been performed. Considering the structure of graphene-coated FeS$_2$ nanoparticles, there are three possible Na$^+$ adsorption sites (Na$_1$: on the graphene, Na$_2$: on the FeS$_2$ surface, and Na$_3$: between FeS$_2$ and graphene), which are displayed in Figure S23a–c in the Supporting Information. From the calculation results, the adsorption energy (E_{ad}) at Na$_1$, Na$_2$, and Na$_3$ sites are 0.35, −1.38, and −3.12 eV, respectively. It has the lowest E_{ad} on the Na$_3$ site, indicating the Na$^+$ tends to be preferentially stored in the FeS$_2$/graphene heterointerface, which will facilitate the Na$^+$ storage based on this interface effect, thus resulting in an enhanced Na$^+$ storage capacity (capacitance effect). On the other side, this phenomenon also well confirms the previous results regarding the surface-limited (capacitance effect) and diffusion-controlled (battery) properties. The DOS of FeS$_2$/carbon materials is nearly with no obvious change after the Na$^+$ insertion (Figure S23d,e, Supporting Information), indicating the superstability of the materials for application in energy storage devices. In addition, the diffusion barrier energy (**Figure 8**) indicates that Na$^+$ migrates under the FeS$_2$/graphene heterointerface easier than single FeS$_2$ surface, which ensures a positive effect of graphene and results in enhanced electrochemical performance for energy storage.

3. Conclusions

In summary, we have successfully prepared the FeS$_2$@graphene@carbon nanofibers anode materials. It was found that the graphene-coating can modify the surface morphology and improve the conductivity. The anode materials displayed inspiring reversible capacity for SIBs (305.5 mAh g^{-1} at 3 A g^{-1} after 2450 cycles) and PIBs (120 mAh g^{-1} at 1 A g^{-1} after 680 cycles) half-cells at room temperature. Surprisingly, the composites can obtain 250 and 200 mAh g^{-1} even at 0 and −20 °C for SIBs, and they can tolerate drastic temperature changes. When included in the FeS$_2$//Na$_2$V$_3$(PO$_4$)$_3$ full-cells, the devices delivered capacity of 102 mAh g^{-1} at 1 C (based on the cathodes) with the energy density of 169 Wh kg^{-1} and the power density of 88 W kg^{-1}. The full-cells also exhibited 50 and 43 mAh g^{-1} at 0 and −20 °C, and the corresponding energy density is 58.7 and 50.1 Wh kg^{-1}, respectively. The DFT calculations indicate that the graphene/FeS$_2$ heterointerface can improve the Na$^+$ storage stability and effectively decrease the Na$^+$ diffusion barrier. Hence, the high Na$^+$/K$^+$ storage properties of FeS$_2$@graphene@carbon nanofibers can be attributed to the high conductivity and fast reaction-diffusion kinetics arising from graphene. Thus, FeS$_2$ as anodes and Na$_3$V$_2$(PO$_4$)$_3$ as cathodes full-cells reflect potential application ability especially at low temperature.

Supporting Information

Supporting Information is available from the Wiley Online Library or from the author.

[1] a) J. Qian, C. Wu, Y. Cao, Z. Ma, Y. Huang, X. Ai, H. Yang, *Adv. Energy Mater.* **2018**, *8*, 1702619; b) D. Su, A. McDonagh, S. Z. Qiao, G. Wang, *Adv. Mater.* **2017**, *29*, 1604007; c) Q. Wang, W. Zhang, C. Guo, Y. Liu, C. Wang, Z. Guo, *Adv. Funct. Mater.* **2017**, *27*, 1703390; d) C. Wang, F. Wang, Z. Liu, Y. Zhao, Y. Liu, Q. Yue, H. Zhu, Y. Deng, Y. Wu, D. Zhao, *Nano Energy* **2017**, *41*, 674; e) Z. Sun, J. Zhang, L. Yin, G. Hu, R. Fang, H.-M. Cheng, F. Li, *Nat. Commun.* **2017**, *8*, 14627; f) S. Qiu, L. Xiao, M. L. Sushko, K. S. Han, Y. Shao, M. Yan, X. Liang, L. Mai, J. Feng, Y. Cao, *Adv. Energy Mater.* **2017**, *7*, 1700403; g) C. Liu, C. Zhang, H. Fu, X. Nan, G. Cao, *Adv. Energy Mater.* **2017**, *7*, 1601127; h) L. Wang, G. Zhang, Q. Liu, H. Duan, *Mater. Chem. Front.* **2018**, *2*, 1414; i) K. Amine, I. Belharouak, Z. Chen, T. Tran, H. Yumoto, N. Ota, S.-T. Myung, Y.-K. Sun, *Adv. Mater.* **2010**, *22*, 3052.

[2] W. Wang, B. Jiang, C. Qian, F. Lv, J. Feng, J. Zhou, K. Wang, C. Yang, Y. Yang, S. Guo, *Adv. Mater.* **2018**, *30*, 1801812.

[3] Y. Dong, Z. S. Wu, S. Zheng, X. Wang, J. Qin, S. Wang, X. Shi, X. Bao, *ACS Nano* **2017**, *11*, 4792.

[4] Z. Jian, S. Hwang, Z. Li, A. S. Hernandez, X. Wang, Z. Xing, D. Su, X. Ji, *Adv. Funct. Mater.* **2017**, *27*, 1700324.

[5] a) B. Ruan, H. Guo, Y. Hou, Q. Liu, Y. Deng, G. Chen, S. Chou, H. Liu, J. Wang, *ACS Appl. Mater. Interfaces* **2017**, *9*, 37682; b) Z. Huang, Z. Chen, S. Ding, C. Chen, M. Zhang, *Solid State Ionics* **2018**, *324*, 267.

[6] a) C. Chen, Y. Yang, S. Ding, Z. Wei, X. Tang, P. Li, T. Wang, G. Cao, M. Zhang, *Energy Storage Mater.* **2018**, *13*, 215; b) G. Ma, K. Huang, J.-S. Ma, Z. Ju, Z. Xing, Q.-C. Zhuang, *J. Mater. Chem. A* **2017**, *5*, 7854; c) Y. Xu, C. Zhang, M. Zhou, Q. Fu, C. Zhao, M. Wu, Y. Lei, *Nat. Commun.* **2018**, *9*, 1720.

[7] a) S. Zhu, J. Li, X. Deng, C. He, E. Liu, F. He, C. Shi, N. Zhao, *Adv. Funct. Mater.* **2017**, *27*, 1605017; b) H. Su, S. Jaffer, H. Yu, *Energy Storage Mater.* **2016**, *5*, 116.

[8] a) M. He, M. Walter, K. V. Kravchyk, R. Erni, R. Widmer, M. V. Kovalenko, *Nanoscale* **2015**, *7*, 455; b) X. Tang, Y. Wei, H. Zhang, F. Yan, M. Zhuo, C. Chen, P. Xiao, J. Liang, M. Zhang, *Electrochim. Acta* **2015**, *186*, 223.

[9] a) Z. Li, L. Zhang, X. Ge, C. Li, S. Dong, C. Wang, L. Yin, *Nano Energy* **2017**, *32*, 494; b) M. Sun, H. Liu, J. Qu, J. Li, *Adv. Energy Mater.* **2016**, *6*, 1600087.

[10] X. Xu, W. Liu, Y. Kim, J. Cho, *Nano Today* **2014**, *9*, 604.

[11] a) T. Evans, D. M. Piper, S. C. Kim, S. S. Han, V. Bhat, K. H. Oh, S. H. Lee, *Adv. Mater.* **2014**, *26*, 7386; b) Y. Xiao, J.-Y. Hwang, I. Belharouak, Y.-K. Sun, *ACS Energy Lett.* **2017**, *2*, 364.

[12] Z. Liu, T. Lu, T. Song, X.-Y. Yu, X. W. D. Lou, U. Paik, *Energy Environ. Sci.* **2017**, *10*, 1576.

[13] K. Zhang, M. Park, L. Zhou, G. H. Lee, J. Shin, Z. Hu, S. L. Chou, J. Chen, Y. M. Kang, *Angew. Chem., Int. Ed.* **2016**, *55*, 12822.

[14] Z. Hu, Z. Zhu, F. Cheng, K. Zhang, J. Wang, C. Chen, J. Chen, *Energy Environ. Sci.* **2015**, *8*, 1309.

[15] a) J. He, Q. Li, Y. Chen, C. Xu, K. Zhou, X. Wang, W. Zhang, Y. Li, *Carbon* **2017**, *114*, 111; b) Y. Zhu, X. Fan, L. Suo, C. Luo, T. Gao, C. Wang, *ACS Nano* **2016**, *10*, 1529; c) Y. Zhu, L. Suo, T. Gao, X. Fan, F. Han, C. Wang, *Electrochem. Commun.* **2015**, *54*, 18; d) W. Chen, S. Qi, M. Yu, X. Feng, S. Cui, J. Zhang, L. Mi, *Electrochim. Acta* **2017**, *230*, 1; e) Z. Lu, N. Wang, Y. Zhang, P. Xue, M. Guo, B. Tang, Z. Bai, S. Dou, *Electrochim. Acta* **2018**, *260*, 755; f) W. Chen, S. Qi, L. Guan, C. Liu, S. Cui, C. Shen, L. Mi, *J. Mater. Chem. A* **2017**, *5*, 5332; g) D. T. Pham, J. P. Baboo, J. Song, S. Kim, J. Jo, V. Mathew, M. H. Alfaruqi, B. Sambandam, J. Kim, *Nanoscale* **2018**, *10*, 5938.

[16] a) Y. Tan, K. W. Wong, Z. Zhang, K. M. Ng, *Nanoscale* **2017**, *9*, 19408; b) E. Shangguan, L. Guo, F. Li, Q. Wang, J. Li, Q. Li, Z. Chang, X.-Z. Yuan, *J. Power Sources* **2016**, *327*, 187; c) S. Seefeld, M. Limpinsel, Y. Liu, N. Farhi, A. Weber, Y. Zhang, N. Berry, Y. J. Kwon, C. L. Perkins, J. C. Hemminger, R. Wu, M. Law, *J. Am. Chem. Soc.* **2013**, *135*, 4412.

[17] S. Wei, S. Xu, A. Agrawral, S. Choudhury, Y. Lu, Z. Tu, L. Ma, L. A. Archer, *Nat. Commun.* **2016**, *7*, 11722.

[18] a) Y. Qiao, M. Ma, Y. Liu, S. Li, Z. Lu, H. Yue, H. Dong, Z. Cao, Y. Yin, S. Yang, *J. Mater. Chem. A* **2016**, *4*, 15565; b) K. N. Chaudhari, M. Y. Song, J.-S. Yu, *Small* **2014**, *10*, 2625.

[19] a) D. Usachov, A. Fedorov, O. Vilkov, B. Senkovskiy, V. K. Adamchuk, L. V. Yashina, A. A. Volykhov, M. Farjam, N. I. Verbitskiy, A. Grueneis, C. Laubschat, D. V. Vyalikh, *Nano Lett.* **2014**, *14*, 4982; b) Y. Zhao, J. Liang, C. Wang, J. Ma, G. G. Wallace, *Adv. Energy Mater.* **2018**, *8*, 1702524.

[20] a) D. Sun, D. Ye, P. Liu, Y. Tang, J. Guo, L. Wang, H. Wang, *Adv. Energy Mater.* **2018**, *8*, 1702383; b) Y. E. Zhu, L. Yang, J. Sheng, Y. Chen, H. Gu, J. Wei, Z. Zhou, *Adv. Energy Mater.* **2017**, *7*, 1701222.

[21] a) Z. Shadike, Y.-N. Zhou, F. Ding, L. Sang, K.-W. Nam, X.-Q. Yang, Z.-W. Fu, *J. Power Sources* **2014**, *260*, 72; b) Y. Chen, X. Hu, B. Evanko, X. Sun, X. Li, T. Hou, S. Cai, C. Zheng, W. Hu, G. D. Stucky, *Nano Energy* **2018**, *46*, 117.

[22] A. Douglas, R. Carter, L. Oakes, K. Share, A. P. Cohn, C. L. Pint, *ACS Nano* **2015**, *9*, 11156.

[23] a) X. Wei, W. Li, J.-A. Shi, L. Gu, Y. Yu, *ACS Appl. Mater. Interfaces* **2015**, *7*, 27804; b) W. Zhao, C. Guo, C. M. Li, *J. Mater. Chem. A* **2017**, *5*, 19195; c) C. Wang, Y. Niu, J. Jiang, Y. Chen, H. Tian, R. Zhang, T. Zhou, J. Xia, Y. Pan, S. Wang, *Nano Energy* **2018**, *45*, 432; d) Y.-X. Wang, J. Yang, S.-L. Chou, H. K. Liu, W.-X. Zhang, D. Zhao, S. X. Dou, *Nat. Commun.* **2015**, *6*, 8689.

[24] a) P. Simon, Y. Gogotsi, B. Dunn, *Science* **2014**, *343*, 1210; b) M. Okubo, E. Hosono, J. Kim, M. Enomoto, N. Kojima, T. Kudo, H. Zhou, I. Honma, *J. Am. Chem. Soc.* **2007**, *129*, 7444.

[25] a) J. Xie, J. Zhu, N. Zhuang, H. Lei, W. Zhu, Y. Fu, M. S. Javed, J. Li, W. Mai, *Nanoscale* **2018**, *10*, 17092; b) Y. Zhao, J. Zhu, S. J. H. Ong, Q. Yao, X. Shi, K. Hou, Z. J. Xu, L. Guan, *Adv. Energy Mater.* **2018**, *8*, 1802565.

[26] a) Z. Xing, Z. Jian, W. Luo, Y. Qi, C. Bommier, E. S. Chong, Z. Li, L. Hu, X. Ji, *Energy Storage Mater.* **2016**, *2*, 63; b) X. Tong, F. Zhang, B. Ji, M. Sheng, Y. Tang, *Adv. Mater.* **2016**, *28*, 9979.

[27] S. Li, P. Ge, C. Zhang, W. Sun, H. Hou, X. Ji, *J. Power Sources* **2017**, *366*, 249.

[28] a) X. Xie, Z. Ao, D. Su, J. Zhang, G. Wang, *Adv. Funct. Mater.* **2015**, *25*, 1393; b) C. Cui, Z. Wei, G. Zhou, W. Wei, J. Ma, L. Chen, C. Li, *J. Mater. Chem. A* **2018**, *6*, 7088.